Simultaneously Improved Reversibility and Hydrogen Production of Solid Oxide Cells Through Infiltrating Air Electrode

Journal:	*Journal of Materials Chemistry A*
Manuscript ID	TA-ART-10-2024-007083.R1
Article Type:	Paper
Date Submitted by the Author:	13-Dec-2024

Complete List of Authors:	Fan, Yueying; National Energy Technology Laboratory; Leidos Inc Chen, Yun; West Virginia University, Mechanical and Aerospace Engineering; National Energy Technology Laboratory Pineault, Richard; National Energy Technology Laboratory Abernathy, Harry; National Energy Technology Laboratory Song, Xueyan; West Virginia University, Mechanical and Aerospace Engineering Kalapos, Thomas; National Energy Technology Laboratory; Leidos Inc

ARTICLE

Simultaneously Improved Reversibility and Hydrogen Production of Solid Oxide Cells Through Infiltrating Air Electrode

Received 00th January 20xx,
Accepted 00th January 20xx

DOI: 10.1039/x0xx00000x

Yueying Fan [a, b, *], Yun Chen [a, c], Richard Pineault [a], Harry Abernathy [a, *], Xueyan Song [a, c], Thomas Kalapos [a, b]

Among the various fuel cells, Solid oxide cells (SOCs) are the unique type that can principally operate reversibly as either fuel cells to produce electricity or as an electrolyser to split water and produce green hydrogen (H_2). Nevertheless, the SOCs' reversibility presents enormous challenges that are manifested by the fast degradation through the cycling between fuel cell and electrolysis mode. While the $La_{0.8}Sr_{0.2}MnO_3$/yttria-stabilized zirconia (LSM/YSZ) air electrode possesses significant advantages in terms of high electrical conductivity and high thermal stability under fuel cell mode, the SOCs with the LSM/YSZ air electrode experience rapid performance degradation with catastrophic electrode delamination shortly after switching from fuel cell to electrolysis mode. To prevent such catastrophic delamination and enable the electrolysis H_2 production, a chemical solution with the designed chemistry of $SrFe_2O_{4-d}$ was infiltrated into the LSM/YSZ air electrode. The infiltration immediately mitigates the catastrophic delamination, and the infiltrated cells exhibit significantly improved reversibility upon the electrochemical operation. Nanostructure examination reveals nanoscale cracks and second-phase nanograins formed in the air electrode from the baseline cell. By contrast, no delamination was observed at either the micron or the nanoscale for the infiltrated cell, which is attributed to the increased ion conductivity of the Fe-doped LSM mixed conductor induced by the significant interdiffusion between the LSM backbone and infiltrates. This study presents a viable method for preventing electrode delamination while enhancing the durability of H_2 production and power generation for reversible fuel cell/electrolysis cell operation. It further opens new research directions of modifying the electrochemical activity of the electrode of inherently functional cells through the infiltration of the solutions with different chemistry.

Introduction

The share of renewable energy, such as solar and wind, is expected to increase from 25% in 2018 to over 40% by 2040, aiming to reduce reliance on fossil fuels and mitigate greenhouse gas emissions.[1] The intermittent nature of renewable energy sources presents significant challenges for electricity systems in maintaining a balanced and consistent power supply. This issue is particularly critical for smaller or more isolated sections of the electric grid that rely heavily on renewable energy systems, as wind and solar power are strongly dependent on weather conditions.[2] Therefore, it is essential to develop energy storage systems or versatile energy conversion systems that can store electrical energy as fuels and reversibly generate electricity on demand. This approach would help balance the grid, reduce the peak demand stress, and increase the share of renewable energy.

Solid oxide cells (SOCs) can primarily function as fuel cells by oxidizing a fuel to produce electricity or as electrolysis cells by electrolyzing water to produce hydrogen (H_2) and oxygen gases. A solid oxide fuel cell (SOFC), as an energy conversion device, efficiently converts the chemical energy stored in fuel such as H_2, hydrocarbons, and biofuels into electrical energy through the electrochemical oxidation of fuels. In this process, the oxygen reduction reaction produces oxygen ions in the air electrode, which are driven by the chemical potential between the air electrode and the H_2 electrode. These oxygen ions then migrate through a dense oxygen-ion-conducting electrolyte such as yttria-stabilized zirconia (YSZ) to the H_2 electrode, where they are consumed by oxidation of fuels to generate electricity. Meanwhile, a solid oxide electrolysis cell (SOEC) converts electrical power into chemically stored energy, such as H_2. In this process, steam is oxidized at the H_2 electrode to produce pure H_2. The produced oxygen ions in the H_2 electrode then migrate back to the oxygen electrode side and produce oxygen.[3-5]

Reversible SOFC/SOEC (R-SOFC/SOEC) systems, capable of both SOFC mode for power generation and SOEC mode for energy storage within a single reactor, have garnered significant attention due to their potential to be cost-effective, highly efficient, and promising for electrical energy storage technology [6-8] in multi-energy distributed systems. However, the application of an R-SOFC/SOEC system within the energy grid faces challenges concerning long-term stability, as the R-SOFC/SOEC

---

[a] National Energy Technology Laboratory, 3610 Collins Ferry Road, Morgantown, WV 26505, USA. Email: Yueying.Fan@netl.doe.gov.
[b] NETL Support Contractor, 3610 Collins Ferry Road, Morgantown, WV 26505, USA.
[c] Department of Mechanical and Aerospace Engineering, West Virginia University, 1306 Evansdale Drive, Morgantown, WV 26506, USA.
*Corresponding Author

operation involves both the SOFC and SOEC operation, potentially leading to more severe performance degradation.

One of the most critical challenges for commercial application of SOEC technology is the long-term degradation of the cell's performance. Key factors include the formation of porosity in the YSZ grain boundaries and grain boundary fracture in the electrolyte,[9] irreversible nickel (Ni) mobility,[10] and depletion of Ni away from[10-12] or toward[13] the electrolyte due to the formation of $Ni(O.H.)_x$ under high operational temperature, high current density and high potential in the H_2 electrode. Additionally, the catastrophic delamination of the air electrode from the electrolyte poses a significant challenge for the commercial application of SOEC technology.[10,14-21] For instance, $La_{0.8}Sr_{0.2}MnO_3$ (LSM) is widely used as the air electrode for SOFC due to its high electrical conductivity, strong catalytic activity for oxygen oxidation, and chemical thermal compatibility with the YSZ electrolyte, and cost-effective manufacturing process. Despite LSM-based cells demonstrating excellent long-term stability under SOFC operation, they face significant challenges in SOEC operation, particularly short-term stability issues caused by the lower oxygen ionic conductivity of the LSM backbone.[22] This limitation can result in high oxygen partial pressure at the air electrode/electrolyte interface, leading to delamination of the LSM from the electrolyte.[21] Addressing these challenges, especially the delamination of the air electrode, is crucial for the advancement of SOEC technology.

Our promising solution is the infiltration of nanoparticles into the air[23-28] or H_2 electrodes.[28,29] This method has proven to be cost-effective and enhances the performance of electrodes by improving microstructure, catalytic activity, and ionic/electronic conductivity, thereby increasing the cell's stability and reliability.[23-25] The fine dispersion of nanoparticles enhances the electrode surface activity without the need for high-temperature treatment typically required for composite electrodes. However, traditional nano-infiltration[26,29-33] methods often fail to prevent delamination at the internal interface between the electrode and the electrolyte.

In contrast, commercial SOFC technology relies on established material chemistries and heat treatment processing. To match or exceed the performance of LSM or lanthanum strontium cobalt ferrite (LSCF), new materials with high conductivity, catalytic activity, thermal expansion compatibility with YSZ, and long-term stability at high temperatures are needed but have yet to be reported. Therefore, modifying the chemistry of the porous electrode phases, particularly the backbone structure and conductivity, presents a promising approach for advancing R-SOFC/SOEC technology. Infiltration materials must meet strict criteria, including low-cost for large-scale applications, maintenance of the catalytic surface activity, electrical and ionic conductivity and with ensuring the backbone's structural integrity during high-temperature SOEC electrochemical operations.

$SrFe_2O_{4-d}$ is a mixed ionic and electronic conductor [34] and is highly suitable for high-temperature applications in SOFC and SOEC due to its dual capability to transport oxygen ions and electrons. Its layered perovskite-related crystal structure facilitates ion migration and electronic conduction. The material exhibits high electronic conductivity, driven by Fe ions in mixed oxidation states (Fe^{3+}/Fe^{2+}), which enable electron hopping. Additionally, its oxygen ionic conductivity, arising from oxygen vacancies, allows ion transport, although it is lower than traditional ionic conductors such as YSZ. Infiltrating $SrFe_2O_{4-d}$ into the air electrode of LSM/YSZ cells has been shown to significantly enhance electrochemical performance by introducing additional pathways for oxygen ion and electron transport, improving the conductivity network. This process also increases the TPB density, facilitating superior oxygen reduction reaction kinetics. Furthermore, $SrFe_2O_{4-d}$ infiltration reduces polarization resistance, refines surface chemistry, and improves the microstructure, establishing it as an excellent catalyst and functional material for enhancing the durability and efficiency of SOFC and SOEC operations.[21, 24]

Stability improvements in reversible SOFC/SOEC systems also remain a critical research focus, particularly for LSM/YSZ cells, which exhibit superior long-term stability compared to LSCF/SDC cells under SOFC operation. Recent studies have demonstrated the infiltration of $Sm_{0.5}Sr_{0.5}CoO_{3-d}$ and $Sm_{0.2}Ce_{0.8}O_{1.9}$ nanoparticles into LSM/YSZ cells significantly enhances stability during high-temperature cycling.[35] Additionally, $(Bi_{0.75}Y_{0.25})_{0.93}Ce_{0.07}O_{1.5-d}$-LSM oxygen electrodes have shown lower degradation rates under reversible SOFC/SOEC conditions, outperforming LSCF-based electrodes.[36] Promising advancements have also been reported in nanocomposite air electrodes, like $Ce_{0.8}Gd_{0.2}O_{1.9}$/LSM, which deliver excellent stability and performance over reversible operations.[37] These findings emphasize the critical role of advanced materials and innovative electrode designs for achieving durable and efficient SOFC-SOEC systems.

This study explores the impact of infiltrating a chemical solution with a nominal composition of $SrFe_2O_{4-d}$ on the reversibility of commercial SOCs. The findings indicate that solution infiltration simultaneously mitigates delamination, enhances fuel cell power density, and reduces electricity consumption in electrolysis cells. The present investigation details how air-electrode infiltration affects both fuel cell and electrolysis mode operation, validate the interaction between the solution and the electrode backbone and clarifies the nanostructure and chemistry origin behind the improved reversibility of the nanostructure.

Experiment

Infiltration of $SrFe_2O_{4-d}$ chemical solution into the air electrode and electrochemical performance evaluation of infiltrated and baseline LSM/YSZ cells under the R-SOFC/SOEC operation

Commercial LSM/YSZ cells were obtained from Nexceris. A comprehensive description of the as-received Nexceris button cells and the infiltration of $SrFe_2O_{4-d}$ chemical solution into the air electrode were described in our previous study.[21]

Performance and stability evaluation of both baseline and $SrFe_2O_{4-d}$ infiltrated LSM/YSZ cells under the R-SOFC/SOEC operation were conducted using a test stand equipped with a bubbler humidifier. Platinum (Pt) meshes (90% platinum/10% rhodium, Unique Wire Weaving, Hillside, NJ) were used for electrode contact, and mica gaskets (Asheville-Schoonmaker Mica, Newport News, VA) served as electrode sealants. For the electrochemical operation, Pt mesh with Ni pastes and Pt mesh with Pt paste were used for fuel electrode and air electrode lead connections, respectively. The cells were initially heated to 800 °C with 400 sccm N_2 flowing to the H_2 electrode and 400 sccm air to the air electrode. Once the temperature stabilized, 400 sccm of 10% dry H_2 balanced with N_2 was introduced to the H_2 electrode until the open circuit voltage (OCV) reached 0.9 V after 1 hour. Subsequently, the dry H_2 concentration was increased to 50%, and the OCV rose to approximately 1 V after 2 hours. Finally, 100% H_2 was supplied to the H_2 electrode with a flow rate of 400 sccm. After 2 hours of exposure to 100% H_2, the OCV stabilized around 1.15 V. All tested cells had OCVs exceeding 1.09 V under dry H_2 at 800 °C, indicating adequate cell sealing. Following this, a constant current density of 0.5 A/cm^2 was applied to the cell for 96 hours in SOFC mode, followed by approximately 96 hours in SOEC mode under 0.5 A/cm^2, 60% steam, and 10% H_2 balance with N_2 at the H_2 electrode. Each time the operational mode was switched, the OCV under SOFC or SOEC was allowed to stabilize for at least 1 hour before applying the current.

During the SOFC operation, impedance spectra were recorded every 24 hours under various direct current (D.C.) bias currents (0-1.0 A/cm^2) with a frequency range of 0.05 Hz to 100 kHz and a perturbation amplitude of 10-75 mA using a frequency response analyzer (Solartron 1252A) and a potentiostat/galvanostat (Solartron 1470E). Impedance spectra and resistance (Ro and Rp) reported in the following sections were measured under the D.C. bias current of 0.5 A/cm^2. For SOEC operation, the steam concentration was maintained at 60% by bubbling the mixture of H_2 and N_2 through a sealed tank with heated DI water (87 °C). The gases were directed to the electrodes and heat-traced at 130 °C to prevent steam condensation. Electrochemical impedance spectra (EIS) were used to characterize the cell's electrochemical properties under 0 A/cm^2 for OCV and potential values of 0.2 V and 0.4 V above OCV. EIS measurements were conducted every 24 hours for both SOFC and SOEC cycles. All the impedance spectra and resistance reported in this paper were measured under the potential of 0.2 V above OCV for the SOEC operation.

To examine the nanostructure of the Ni/YSZ fuel electrode without the electrochemical operation, a baseline cell was reduced, and the fuel electrode was thermally exposed to a H_2O:H_2 mixture with the ratio 30%/70% at 800 °C for 500 hours.

Nanostructure studies before and after the R-SOFC/SOEC operation

The nanostructure of the as-received and post-tested electrodes, including both H_2 and air electrodes, was analysed by transmission electron microscopy (TEM) coupled with energy-dispersive spectroscopy (EDS). All the TEM examinations focused on the active layer of the electrodes. Mechanical polishing and ion milling in a liquid-nitrogen-cooled holder were used for sample preparation. TEM imaging, electron diffraction, and diffraction contrast analyses were performed with a JEM-2100 TEM (JOEL USA, Peabody, MA) operating at 200 kV. Chemical composition analysis was conducted with EDS, which examined a sample area approximately 20 nm in diameter.

Results

Performance improvement and degradation mitigation of the $SrFe_2O_{4-d}$ infiltrated LSM/YSZ cell operated under R-SOFC/SOEC

The electrochemical operation of the cell started from the SOFC mode using 100% H_2 and operated under the constant current density of 0.5 A/cm^2 for 96 hours and then switched to the SOEC mode operated with 0.5 A/cm^2 using 60% steam for another 96 hours. Fig. 1 indicates the cell voltage as the function of operation time under the R-SOFC/SOEC operation for the baseline and $SrFe_2O_{4-d}$ infiltrated LSM/YSZ cells.

The performance of LSM/YSZ baseline cell deteriorated, with a decrease in cell operation voltage of 11.6% after 4 cycles of the R-SOFC/SOEC operation (based on the SOFC cycle voltages). Upon removal of the LSM/YSZ baseline cell after only 4 cycles of the R-SOFC/SOEC operation, visible delamination in the air electrode was observed under the naked eye. In contrast, the $SrFe_2O_{4-d}$ infiltrated cell did not exhibit any visible delamination in the air electrode after 6 cycles of the R-SOFC/SOEC operation. The $SrFe_2O_{4-d}$ infiltration into the air electrode markedly enhanced the cell's performance, particularly during SOEC cycles. Initially, the performance during the first SOFC cycle showed significant improvement after the $SrFe_2O_{4-d}$ infiltration in the air electrode, though some degradation was observed subsequently.

The voltage of the $SrFe_2O_{4-d}$ infiltrated cell increased by 8.9% after four cycles of the R-SOFC/SOEC operation, mainly due to a performance decline in the first SOEC cycle. Overall, the performance of the $SrFe_2O_{4-d}$ infiltrated cell decreased by 17.5% after six cycles of the R-SOFC/SOEC operation. After six cycles,

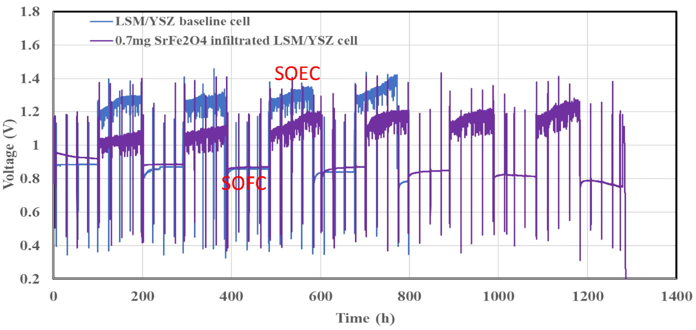

Fig. 1 Performance and degradation of the long-term test under the R-SOFC/SOEC operation for the $SrFe_2O_{4-d}$ infiltrated and baseline LSM/YSZ cells at 800 °C and 0.5 A/cm^2 with 60% steam for the SOEC cycle. Vertical lines correspond to the recording of EIS data.

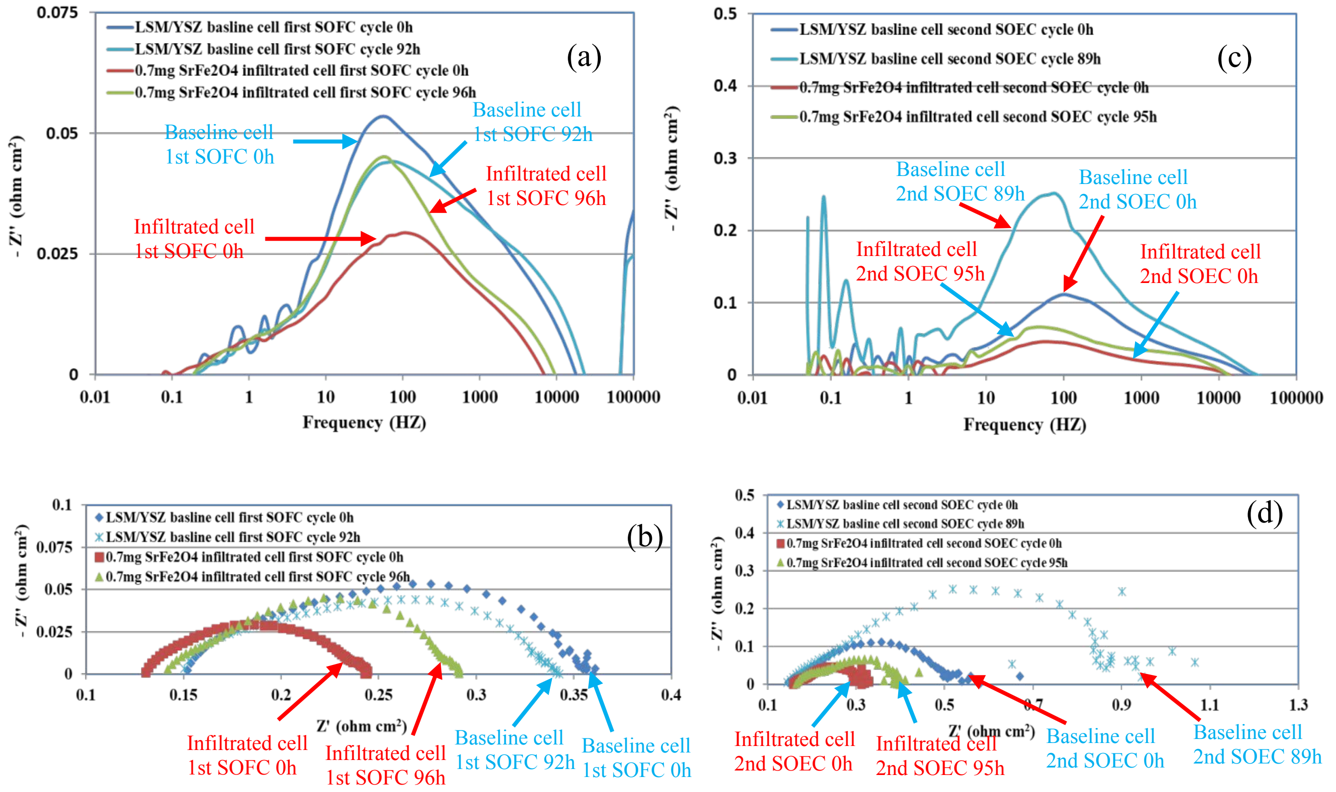

Fig. 2 Comparison of the impedance and ohmic/polarization resistance for the SOFC and SOEC cycles between the $SrFe_2O_{4-d}$ infiltrated and LSM/YSZ baseline cells operated under R-SOFC/SOEC: (a) Bode plot of the SOFC cycles; (b) Nyquist plot of the SOFC cycles; (c) Bode plot of the SOEC cycles; and (d) Nyquist plot of the SOEC cycles.

totalling 1,300 hours, the final SOEC voltage of the infiltrated cell was approximately 1.2 V, comparable to the initial SOEC cycle voltage of the baseline cell at 0 hours. Thus, the $SrFe_2O_{4-d}$ infiltration in the air electrode substantially improved cell performance during SOEC operation and prolonged the operational lifespan of the R-SOFC/SOEC operation without air electrode delamination.

EIS comparison between the baseline and $SrFe_2O_{4-d}$ infiltrated LSM/YSZ cells operated under R-SOFC/SOEC

Fig. 2 (a) and (b) present a comparison of the impedance, as well as the ohmic and polarization resistance, between the $SrFe_2O_{4-d}$ infiltrated and LSM/YSZ baseline cells during the first SOFC cycle at 0 hours and 96 hours. The $SrFe_2O_{4-d}$ infiltration in the air electrode of the LSM/YSZ cell significantly reduced the total impedance of both the air and H_2 electrodes at 0 hours. Even at 96 hours, the impedance of the H_2 electrode in the infiltrated cell remained lower than that of the baseline cell despite $SrFe_2O_{4-d}$ being infiltrated only in the air electrode shown in Fig. 2(a).

The polarization resistance also decreased significantly, as shown in the Nyquist plot in Fig. 2 (b) for both 0 hours and 96 hours. Meanwhile, the ohmic resistance exhibited a slight decrease at both time points due to $SrFe_2O_{4-d}$ infiltration. The introduction of $SrFe_2O_{4-d}$ nanoparticles modified the surface structure and the chemistry of the LSM/YSZ backbone, facilitating more continuous electronic and ionic conduction pathways within the electrode. This changes of the microstructure and chemistry at the LSM/YSZ interface, coupled with an increase in active reaction sites, including the triple phase boundaries (TPBs) for electrochemical reactions, resulted in improved electrochemical performance, evidenced by the reduced ohmic and polarization resistances.

The reduction in impedance and polarization resistance correlated with the performance enhancement observed in the voltage-time plot for the infiltrated cell. However, a distinct trend was noted in Fig. 2 (b): while the polarization resistance of the baseline cell decreased during the first SOFC cycle, the polarization resistance of the infiltrated cell increased slightly. This behaviour during the initial operating period is attributed to structural rearrangements in the LSM air electrode, leading to an increase in the availability of active sites and enhanced catalytic activity for the oxygen reduction reaction (ORR). These structural changes involve a redistribution of ions within the LSM/YSZ structure, improving connectivity, reducing polarization resistance, and optimizing electrochemical performance, particularly within the first 100 hours of SOFC operation. The observed improvements in the infiltrated cell are further attributed to the interdiffusion between Sr and Fe and the LSM backbone. The infiltration of $SrFe_2O_{4-d}$ nanoparticles thus demonstrates its potential to significantly boost the electrochemical performance of LSM/YSZ cells by reducing both ohmic and polarization resistances and optimizing reaction pathways.

Fig. 2 (c) and (d) compare the second SOEC cycle impedance and ohmic/polarization between the $SrFe_2O_{4-d}$ infiltrated and LSM/YSZ baseline cells operated under R-SOFC/SOEC at 0 hours and 90 hours. The impedance of SOEC cycles at 0 hours and 90 hours significantly decreased after the $SrFe_2O_{4-d}$ nanoparticle infiltration in the air electrode compared to the LSM/YSZ baseline cell. The polarization resistance also decreased considerably after infiltration. The decreased impedance and polarization resistance of the $SrFe_2O_{4-d}$ infiltrated LSM/YSZ cell further demonstrated that the $SrFe_2O_{4-d}$ nanoparticles not only increase the active sites for an electrochemically catalytic reaction but also increase triple-phase boundaries in the air electrode, leading to increased oxygen ion conductivity in the air electrode. The decreased impedance and polarization resistance after nanoparticle infiltration in the air electrode of the cell correspondingly caused improved performance during the SOEC cycle operation for the infiltrated cell over the LSM/YSZ baseline cell.

The ohmic/polarization resistance changes of the SOFC cycle for the $SrFe_2O_{4-d}$ infiltrated and LSM/YSZ baseline cells operated under R-SOFC/SOEC are summarized in Fig. 3. The ohmic/polarization resistance of the $SrFe_2O_{4-d}$ infiltrated cell increased more than that of the LSM/YSZ baseline cell with more SOFC cycle operation. The initial ohmic/polarization resistance significantly decreased after the $SrFe_2O_{4-d}$ nanoparticle infiltration in the air electrode of the LSM/YSZ cell compared to the LSM/YSZ baseline cell shown in Fig. 3. The polarization resistance of the $SrFe_2O_{4-d}$ infiltrated cell and LSM/YSZ cell increased by 183.7 mΩ cm^2 and 57 mΩ cm^2 per 1,000 hours, respectively. The ohmic resistance of the $SrFe_2O_{4-d}$ infiltrated cell and LSM/YSZ cell increased by 45.4 mΩ cm^2 and 39.6 mΩ cm^2, respectively. Therefore, both the ohmic and polarization resistance increases contributed to the cell's performance degradation, with polarization resistance increasing more than ohmic resistance increases for the SOFC cycles. The polarization resistance sharply increased in the fifth SOFC cycle for the LSM/YSZ baseline cell. When the baseline cell was taken out, the cell was found to be totally delaminated from the air electrode by the naked eye. Therefore, the sharp increase in the polarization resistance for the LSM/YSZ baseline cell may correspond to the delamination of the air electrode.

$SrFe_2O_{4-d}$ infiltration into the air electrode significantly enhances and prolongs the overall reversible SOFC/SOEC operation, particularly in mitigating delamination at the air electrode, due to the increased catalytic activity and TPBs density introduced by the $SrFe_2O_{4-d}$ nanoparticles. However, the ohmic and polarization resistances of the $SrFe_2O_{4-d}$ infiltrated cell increase more than those of the baseline cell during the SOFC cycles. This is primarily due to the long-term degradation mechanisms associated with the infiltrated $SrFe_2O_{4-d}$ nanoparticles, including sintering of the nanoparticles at high operating temperatures, which reduces their surface area and catalytic activity, and agglomeration, which obstructs ion and electron pathways in the active functional layer. This effect results in greater ohmic resistance increase for $SrFe_2O_{4-d}$ infiltrated cells compared to baseline cells, which do not experience such nanoparticle-induced issue.

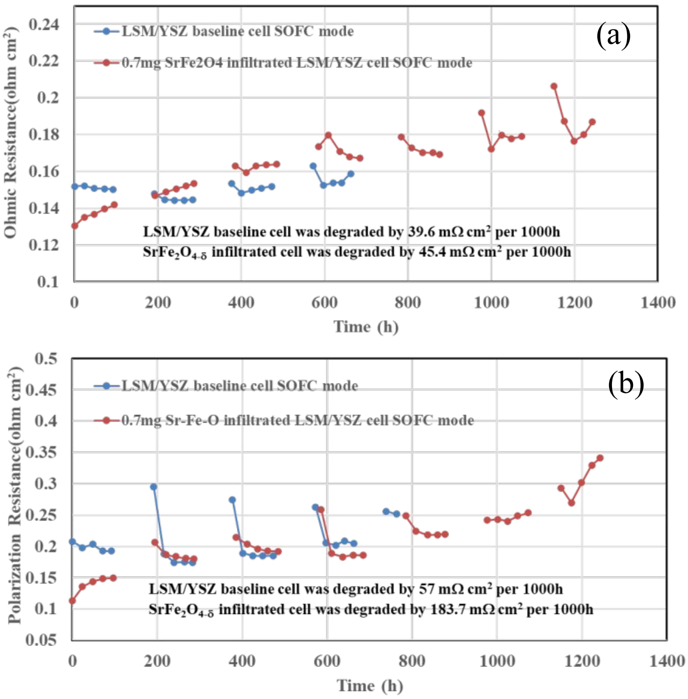

Fig. 3 Ohmic/polarization resistance changes of the SOFC cycles for the $SrFe_2O_{4-d}$ infiltrated and LSM/YSZ baseline cells under the R-SOFC/SOEC operation: (a) Ohmic resistance changes; (b) Polarization resistance changes.

The ohmic/polarization resistance changes of the SOEC cycles for the $SrFe_2O_{4-d}$ infiltrated and LSM/YSZ baseline cells under the R-SOFC/SOEC operation are summarized in Fig. 4. Both the ohmic and polarization resistance of the SOEC cycles for the LSM/YSZ baseline cell increased more than that of the $SrFe_2O_{4-d}$ infiltrated LSM/YSZ cell, despite the ohmic resistance of the $SrFe_2O_{4-d}$ infiltrated LSM/YSZ cell being a little higher than that of the baseline cell during the SOEC operational cycles. The overall ohmic resistance of the SOEC cycles for the $SrFe_2O_{4-d}$ infiltrated and LSM/YSZ cells increased by 43.8 mΩ cm^2 and 102 mΩ cm^2, respectively. The overall polarization resistance of the SOEC cycles for the $SrFe_2O_{4-d}$ infiltrated and LSM/YSZ cells increased by 281 mΩ cm^2 and 1,627 mΩ cm^2 per 1,000 hours, respectively. The ohmic resistance of the baseline cell sharply increased at the fourth SOEC cycle, corresponding to the cell delamination. The ohmic resistance of the LSM/YSZ baseline cell after 4 SOEC cycles increased two times more than that of the infiltrated LSM/YSZ cell after six cycles of the SOEC operation, while the polarization resistance of the LSM/YSZ baseline cell after 4 SOEC cycles increased seven times more than that of the infiltrated LSM/YSZ cell after 6 cycles of the SOEC operation. Even though both ohmic and polarization resistance changes contributed to the cell's performance degradation, the polarization resistance change contributed a lot more than the ohmic resistance to a cell's performance degradation during the SOEC cycles. The overall performance degradation for both infiltrated and baseline cells mainly occurred during the SOEC cycles. The overall polarization resistance of the baseline cell increased by 1,627 mΩ cm^2 during 4 SOEC cycles,

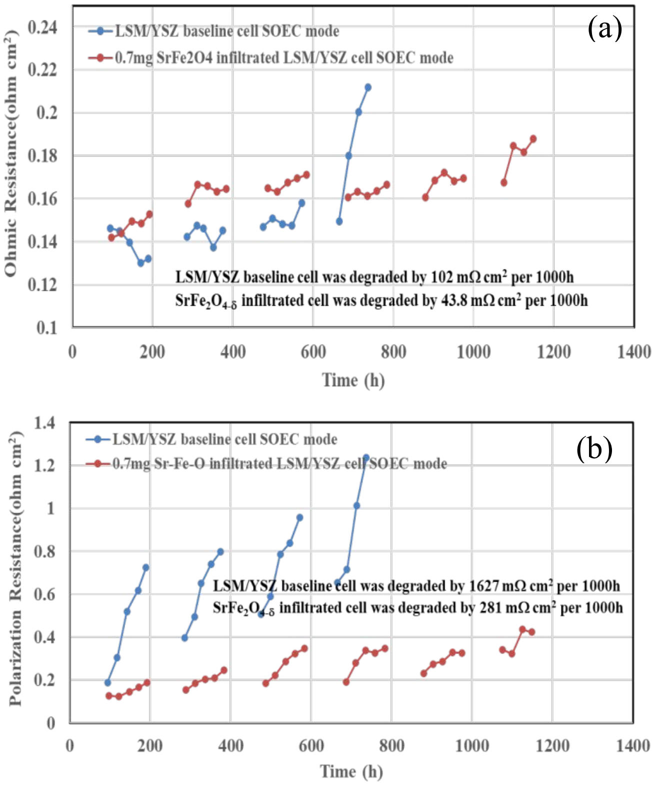

Fig. 4 Ohmic/polarization resistance changes of the SOEC cycles for the $SrFe_2O_{4-d}$ infiltrated and LSM/YSZ baseline cells under the R-SOFC/SOEC operation: (a) Ohmic resistance changes; (b) Polarization resistance changes.

and the cell delaminated in the air electrode after 4 cycles of the R-SOFC/SOEC operation.

SEM/TEM studies of air/H_2 electrodes of the baseline and $SrFe_2O_{4-d}$ infiltrated LSM/YSZ cells before and after R-SOFC/SOEC tests

Fig. 5 shows SEM images of the air electrode of the LSM/YSZ baseline cell before and after the R-SOFC/SOEC operation. Fig. 5 (a) shows an excellent contact in the air electrode/electrolyte interface for the LSM/YSZ baseline cell before the R-SOFC/SOEC test. Catastrophic delamination of the air electrode from the electrolyte for the LSM/YSZ baseline cell after the R-SOFC/SOEC test is shown in Fig. 5 (b) and (c). The representative TEM studies were performed on the left thin layer of the air electrode of the baseline cell after delamination from the electrolyte to understand the nanostructure changes. Fig. 5 (d) and Table 1 show the accumulation of nanograins containing La, Sr, and Mn along the YSZ/YSZ grain boundaries. There were nanoscale cracks along the LSM/LSM grain boundary shown in Fig. 5 (e), and also the LSM/YSZ interface associated with the second phase nanograins and nano cracks are shown in Fig. 5 (f). The crack formation may cause the cell's ohmic resistance to increase, as shown in Fig. 3 and Fig. 4 for both the SOFC and SOEC cycles. The nanograins that formed in the YSZ/YSZ and LSM/YSZ interfaces could be attributed to the accumulated high pressure built into the interface, which broke down the LSM backbone into nano-size pieces due to the low ion conductivity of the LSM backbone. Similarly, the nano cracks that formed in the LSM/LSM and LSM/YSZ interfaces could also be caused by the accumulated high pressure built into the interface due to the low ion conductivity of the LSM, which caused the cell's performance degradation even after the short-term R-SOFC/SOEC operation. With more cycles of the R-SOFC/SOEC test, high pressure and crack built in the interface of the air electrode and electrolyte caused the total delamination of the air electrode from the electrolyte.

Representative SEM/TEM images of the air electrode for the $SrFe_2O_{4-d}$ infiltrated LSM/YSZ cell after the R-SOFC/SOEC test are shown in Fig. 6. The SEM images in Fig. 6 (a) show no delamination between the air electrode and electrolyte for the infiltrated cell even after more R-SOFC/SOEC operation cycles. The $SrFe_2O_{4-d}$ infiltration in the air electrode significantly prevented the delamination of the air electrode from the electrolyte. The TEM studies in Fig. 6 (b) and (c) show that infiltrated nanoparticles are present within the original pore region, in which the $SrFe_2O_{4-d}$ infiltration in the air electrode significantly increased the three-phase boundary. Furthermore, the EDS studies summarized in Table 2 show elements of La and Mn from the LSM backbone diffuse into the infiltrated $SrFe_2O_{4-d}$ nanoparticles, which makes the infiltrated nanoparticle become mixed ion conducting La-Sr-Mn-Fe nanoparticles located on the surface of the LSM and YSZ. Those nanograins have different chemistry, presumably caused by their different distance to the LSM/YSZ grains or the interaction between the infiltrate and the LSM/YSZ backbone. Furthermore, the infiltrated elements of Sr and Fe from the $SrFe_2O_{4-d}$ infiltrates also significantly interact with the LSM backbone and diffuse into the LSM backbone, which causes the LSM backbone to become a well-mixed conductor of Fe-doped LSM. The A-site deficient $(LaSr)(FeMn)O_x$ nano infiltrate grains (with different chemistry) possess electrocatalytic activity toward operation and have increased the number of TPBs. The LSM backbone grain becomes Fe-doped LSM, which possesses substantial ionic conductivity and changes the LSM from an electronic conductor to a mixed conductor. Therefore, the increased ionic conductivity of the LSM backbone could further increase the pathway of oxygen ions, which induces lower polarization resistance and mitigation of performance degradation, especially for the SOEC cycles.

Catalytic Fe-Mn enriched La-Sr-Mn-Fe-O particles sitting on mixed ionic conducting Fe-doped LSM surface are shown in Fig. 6 (d). Such Fe-doped LSM with mixed conductivity could dramatically increase the ionic pathway, decrease the pressure buildup at the electrolyte/electrode interface, and ultimately mitigate the delamination. This increased durability of infiltrated cells may be attributed to a more active oxygen electrode, achieved by solution-based infiltration, to circumvent delamination. Increased activity of the oxygen electrode would limit the oxygen pressure buildup and thus the oxygen-related delamination. Cells with a lower polarization resistance should, in turn, also show better durability toward oxygen electrode delamination, which is consistent with the literature reports such as the Pd into the LSM by infiltration substantially enhances the TPBs and the electrode activity of the LSM electrode for the oxygen evolution reaction (OER) with increased performance and decrease in the delamination.[33]

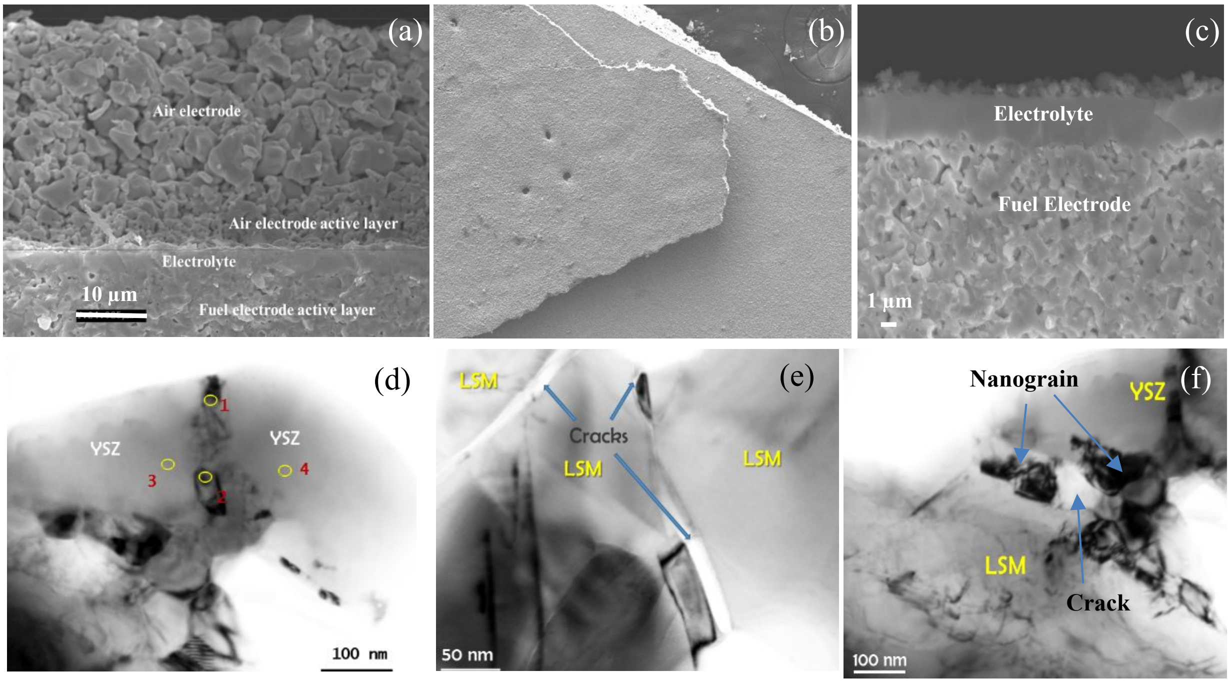

Fig. 5 SEM/TEM studies of the air electrode for the LSM/YSZ baseline cell before and after the R-SOFC/SOEC test: (a) SEM images of the as-received baseline cell without testing; (b) SEM top view of the delaminated baseline cell after testing; (c) SEM cross-section of the delaminated baseline cell after testing; (d) TEM images of the nanograin accumulated in the YSZ/YSZ interface after testing; (e) TEM images of the crack that formed in the LSM/LSM interface after testing; (f) TEM images of the nanograin and crack that formed in the LSM/YSZ interface after testing.

Table 1 EDS of different spots shown in Fig. 5 (d)

At%	O	La	Sr	Mn	Zr	Y	Formula
1	60.85	7.68	1.99	12.10	14.96	2.43	$(La_{0.79}Sr_{0.21})_{0.80}MnO_x$+YSZ
2	68.06	5.24	1.32	7.89	14.99	2.50	$(La_{0.80}Sr_{0.20})_{0.83}MnO_x$+YSZ
3	64.17	0.47		2.02	28.66	4.68	$Zr_{0.80}Y_{0.13}Mn_{0.06}La_{0.01}O_x$
4	67.89	0.42		1.66	25.39	4.64	$Zr_{0.79}Y_{0.14}Mn_{0.05}La_{0.02}O_x$

The TEM studies were conducted on the H_2 electrodes of both the as-received baseline and infiltrated LSM/YSZ cells to examine nano structural changes after R-SOFC/SOEC operation. The TEM images in Fig. 7 (a-1), (a-2), and (a-3) show the as-received cells that had not undergone R-SOFC/SOEC operation but had been thermally exposed to 800°C with 30% steam. These images reveal an intact Ni/YSZ interface and original pore regions without NiO formation, with YSZ grain boundaries remaining intact and free of secondary phases or core-shell structures at the nanoscale. However, after four cycles of R-SOFC/SOEC operation on the baseline cell and six cycles on the infiltrated LSM/YSZ cells, less dense but significantly larger core-shell structures, approximately 50 nm in size, accumulated primarily at the YSZ/YSZ grain boundary junctions,[38] as seen in Fig. 7 (b-1) and (b-2). These changes could lead to increased polarization resistance and subsequent performance degradation. In the core-shell structure at the grain boundaries, the core has vacancy enrichment, and the shell has dopants of Y enrichment. Those core-shell structures result from the space charge layer effect accumulated at the YSZ grain boundaries. Due to the ordering of both the dopants and the vacancies, the core-shell region and the associated grain boundaries are with lower conductivity. The core-shell structures inhibit the transport of oxygen ions and electrons by blocking active TPBs. Additionally, they may create a physical barrier, reducing the efficiency of oxygen adsorption and diffusion. Their dense nature also implies reduced catalytic surface area, further impairing performance.[38]

Additionally, large NiO particles were observed in the original pore regions of the H_2 electrode following R-SOFC/SOEC operation in both the baseline and infiltrated LSM/YSZ cells, as shown in Fig. 7 (c-1) and (c-2). These NiO particles likely formed due to Ni migration during the extended R-SOFC/SOEC tests. A thermodynamic analysis[39] conducted by our group revealed that under polarization, the oxygen partial pressure near the Ni-electrolyte interface can be substantially higher than that at the hydrogen electrode. This can lead to Ni oxidation and an increased concentration of the gaseous $Ni(OH)_2$, which in turn accelerates the transport of Ni. EDS analysis, presented in Table 3, confirmed these

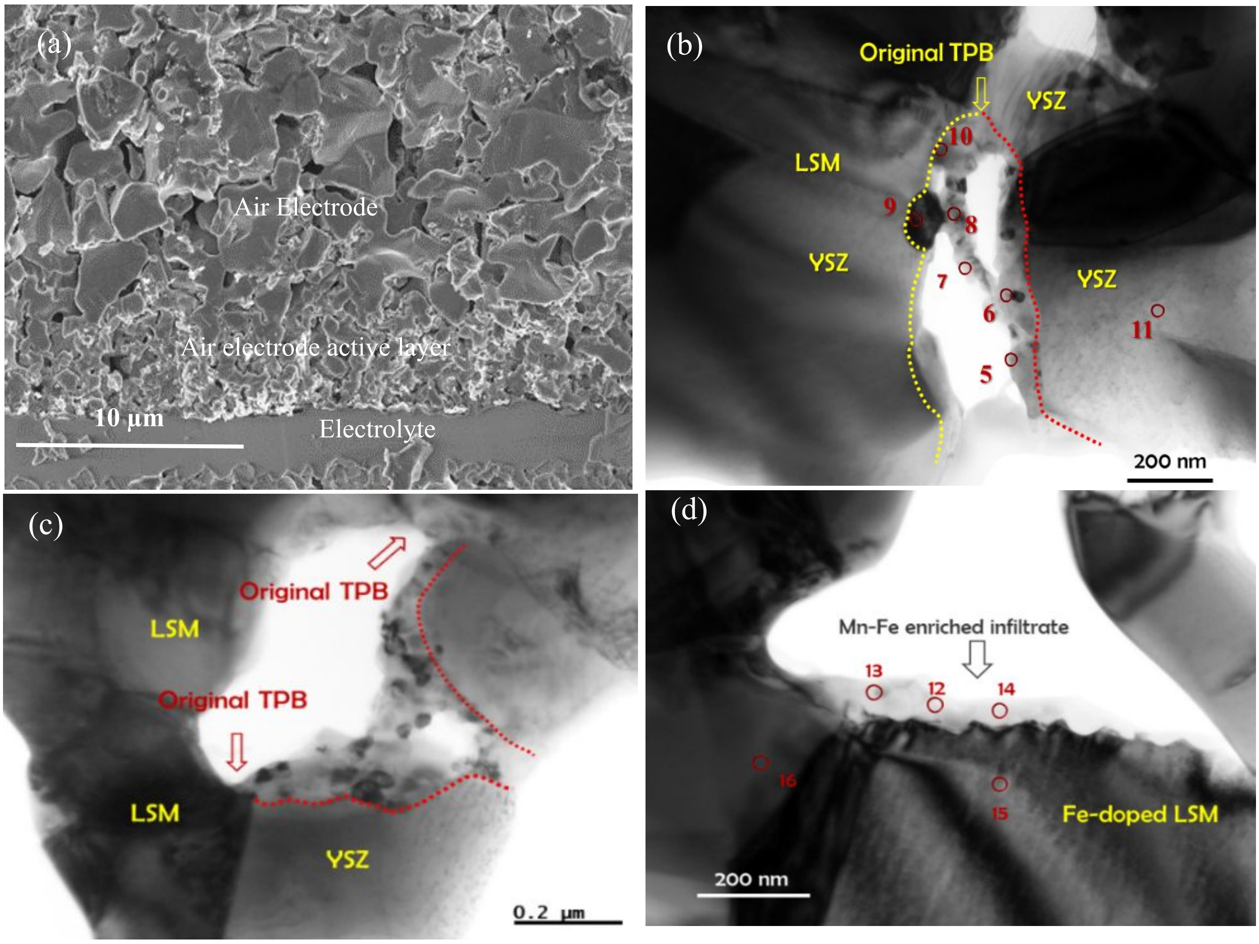

Fig. 6 SEM/TEM studies of air electrode for the $SrFe_2O_{4-d}$ infiltrated LSM/YSZ cell operated under R-SOFC/SOEC: (a) SEM image of intact interface of the air electrode/electrolyte after testing; (b) and (c) TEM images of increased TPB by the $SrFe_2O_{4-d}$ infiltration in the air electrode; (d) Mn-Fe enriched infiltrates on Fe-doped LSM enhanced the oxygen ion conductivity by infiltration in the air electrode.

Table 2 EDS of different spots shown in Fig. 6 (b) and (d)

At%	O	La	Sr	Mn	Fe	Zr	Y	Formula
5	49.12	12.38	10.71	15.07	12.72			$(La_{0.54}Sr_{0.46})_{0.83}(Mn_{0.54}Fe_{0.46})O_x$
6	34.12	17.72	14.33	17.31	16.52			$(La_{0.55}Sr_{0.45})_{0.95}(Mn_{0.51}Fe_{0.49})O_x$
7	64.71	3.53	13.66	9.84	8.26			$(La_{0.21}Sr_{0.79})_{0.95}(Mn_{0.54}Fe_{0.46})O_x$
8	58.39	3.25	16.01	10.94	11.42			$(La_{0.17}Sr_{0.83})_{0.84}(Mn_{0.49}Fe_{0.51})O_x$
9	62.47					31.11	6.42	$Y_{0.17}Zr_{0.83}Ox$
10	60.07		3.09	11.52	25.32			$Sr_{0.08}(Mn_{0.31}Fe_{0.69})O_x$
11	34.64			3.21		52.12	10.02	$Y_{0.15}Mn_{0.05}Zr_{0.80}Ox$
12	75.36		2.46	10.51	11.67			$Sr_{0.11}(Mn_{0.48}Fe_{0.52})O_x$
13	72.91	1.07	2.86	10.68	12.48			$(La_{0.27}Sr_{0.73})_{0.17}(Mn_{0.46}Fe_{0.54})O_x$
14	76.14	1.61	3.74	9.29	9.21			$(La_{0.30}Sr_{0.70})_{0.29}(Mn_{0.50}Fe_{0.50})O_x$
15	71.13	9.71	2.82	15.62	0.72			$(La_{0.77}Sr_{0.23})_{0.77}(Mn_{0.96}Fe_{0.04})O_x$
16	68.27	11.71	3.42	15.35	1.24			$(La_{0.77}Sr_{0.23})_{0.91}(Mn_{0.93}Fe_{0.07})O_x$

particles as NiO. Suppose the NiO is reduced back to Ni during SOFC cycles. In that case, this Ni migration might temporarily generate new triple-phase boundaries, potentially explaining the partial recovery of performance during the SOFC cycles after degradation in the SOEC cycle, as illustrated in Fig. 1.

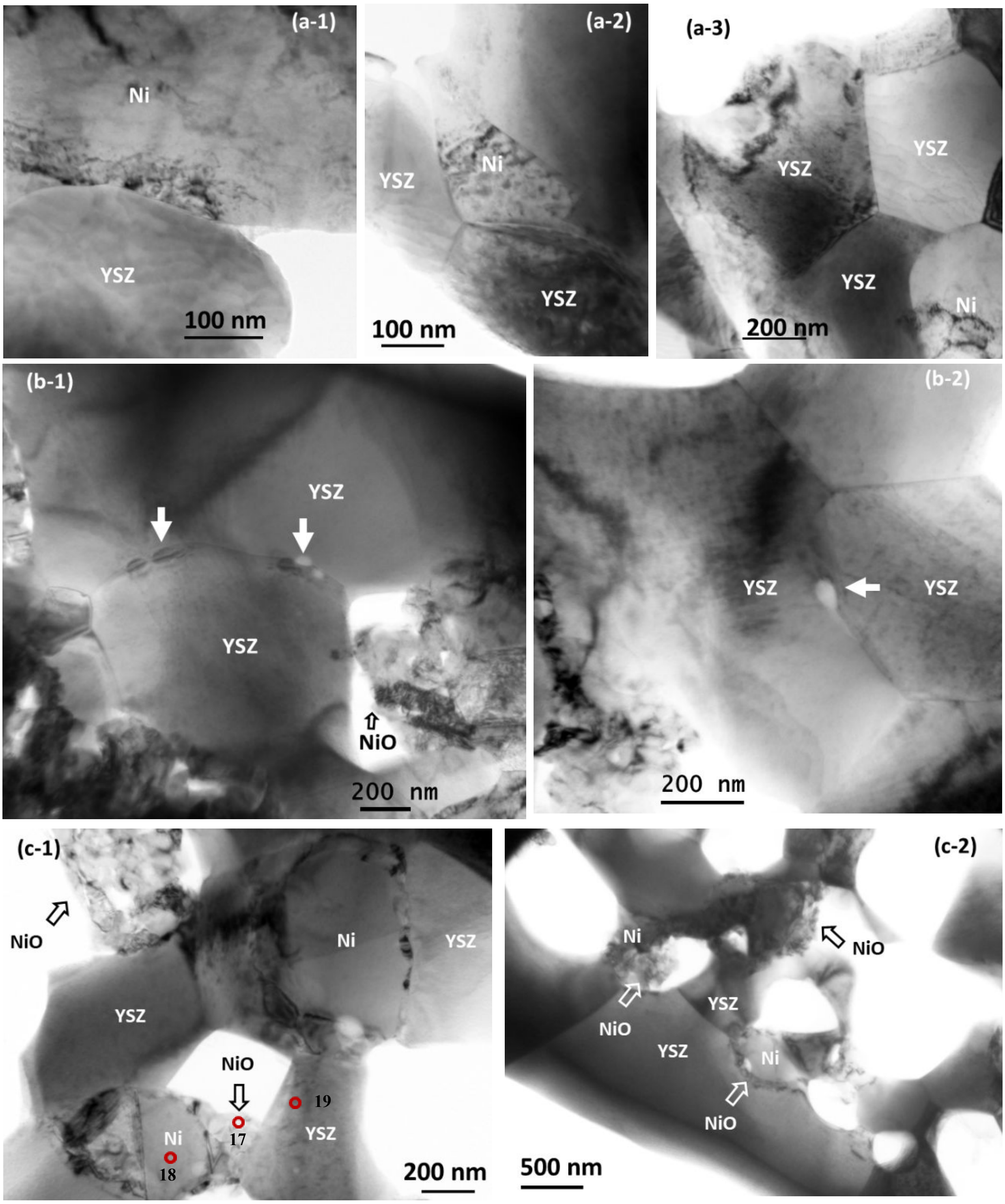

Fig. 7 TEM studies of H_2 electrode for the baseline and $SrFe_2O_{4-d}$ infiltrated LSM/YSZ cells operated under R-SOFC/SOEC: (a-1), (a-2), and (a-3) as-received cell without testing that Ni/YSZ electrode thermally exposed to 800 °C, 30% steam showing the intact Ni/YSZ interface and the original pore region that is lacking the formation of the NiO; (b-1) and (b-2) less dense but much larger core shells with the dimension of ~50 nm accumulated mainly at the YSZ/YSZ grain boundary junctions; (c-1) and (c-2) NiO formation at the original pores of the H_2 electrode after the R-SOFC/SOEC operation for both the baseline cells and infiltrated LSM/YSZ cells.

Table 3 EDS of different spots shown in Fig. 7 (c-1)

At%	O	Zr	Y	Ni	Formula
17	53.57			46.43	NiO_x
18				100	Ni
19	60.42	33.83	5.75		$Zr_{0.85}Y_{0.15}O_x$

Discussion

Increased reversibility induced by solution infiltration of the air electrode

It is worth noting that from the second SOFC cycle onward, the polarization resistance exhibited a significant reduction with the first 24 hours of SOFC operation for both the LSM/YSZ baseline and infiltrated cells shown in Fig. 3 (b), which caused the increased voltage for each SOFC cycle shown in Fig. 1. Therefore, a SOFC cycle may recover some of the performance loss occurred in each SOEC cycle. More detail can be found in Fig. 8 for the EIS spectra of the SOFC and SOEC cycles for both the LSM/YSZ baseline and infiltrated cells. The impedance and polarization resistance of each SOFC cycle at 0 hours was higher than that of the last SOFC cycle at 96 hours for both the baseline and infiltrated cells, which denoted each SOEC cycle caused more performance degradation to the cell shown in Fig. 8 (a), (b), (e), and (f). Beginning with the second SOFC cycle, the impedance and polarization resistance of each SOFC cycle at 96 hours were markedly lower compared to the value observed at the start (0 hour) of each respective SOFC cycle, which corresponded to the increased performance during each SOFC cycle operation shown in Fig. 1. Therefore, SOFC cycles can recover part of the performance loss that occurs in each SOEC cycle, which is consistent with another study[40] that suggested a mechanism of degradation according to which the high oxygen partial pressure at the interface formed during the SOEC mode could be released by the SOFC mode. With more SOFC cycle operations, the ohmic resistance does not increase significantly. However, the impedance and polarization resistance both increased, leading to performance degradation. Fig. 8 (c), (d), (g), and (h) show the EIS spectra of the LSM/YSZ baseline and infiltrated cells for the SOEC cycles during the R-SOFC/SOEC operation, respectively. The impedance and polarization resistance of each SOEC cycle at 0 hours was significantly lower than the last SOEC cycle at 96 hours, which further demonstrated that subsequent SOFC cycle operations recovered part of the performance loss suffered in each SOEC cycle. The impedance and polarization resistance of each SOEC cycle increased. Performance degradation mainly occurred during the SOEC cycle operation, corresponding to the voltage increase during the SOEC cycle operation shown in Fig. 1. With more SOEC cycle operations, the ohmic resistance did not increase. However, the impedance and polarization resistance both increased, contributing to performance degradation.

Performance recovery during each SOFC cycle operation could occur in both air and H_2 electrodes for both the baseline and infiltrated cells. A NiO cluster formed in the original pore of H_2 electrode due to Ni migration during an SOEC operational cycle, which was subsequently reduced to Ni during an SOFC operational cycle, which may increase the TPBs that explain the recovered performance. If irreversible microstructural changes such as fracturing take place in the H_2 electrode shown in Fig. 7 (b), only partial performance recovery during the SOFC operational cycle could occur. In the air electrode, accumulated air pressure due to the low oxygen ion conductivity of the LSM backbone, especially for the baseline cell, could also be released during the SOFC cycle operation before the nano-size crack occurs, shown in Fig. 5 (e), which caused the significant sharp polarization resistance to drop at 0 hours of the SOFC cycle when switching from the SOEC cycle shown in Fig. 3 (b) for the baseline cell. However, the $SrFe_2O_{4-d}$ nanoparticle infiltration in the air electrode of the LSM/YSZ cell significantly increased the oxygen ion conductivity in the air electrode, which mitigated the pressure accumulation due to the increased TPBs in the original pore and the formation of the mixed conductor of Mn-Fe enriched infiltrates located on the Fe-doped LSM backbone. This phenomenon was clearly denoted in Fig. 3 (b) with a lower polarization resistance at 0 hours of each SOFC cycle and a significantly lower polarization resistance in each SOEC cycle for the infiltrated cell shown in Fig. 4 (b). Therefore, the $SrFe_2O_{4-d}$ infiltration in the air electrode significantly increased the reversibility for the LSM/YSZ-based cell, demonstrated by the decreased impedance and polarization for the infiltrated cell shown in Fig. 2 (c) and (d), and improved performance and mitigated performance degradation shown in Fig. 1.

The enhanced conductivity observed in the electrode can be attributed to the decrease in the ohmic resistance in the Nyquist plot, resulting from $SrFe_2O_{4-d}$ infiltration into the air electrode. This improvement in conductivity is accompanied by a reduction in the polarization resistance, which also reflects an enhancement in catalytic activity.

To identify the physical origin of these polarization resistance changes, the dynamic constants within the impedance data were analysed by evaluating the relaxation times and the relaxation amplitudes of the impedance-related processes through deconvolution techniques.[41-44] The DRT analysis shown in Fig.9 reveals two distinct arcs, P3 and P4, corresponding to processes occurring at frequencies in the range of 3-5 Hz and 100-200 Hz, respectively, with the P4 process being dominant. Upon infiltration, the P4 arc shifts toward a higher frequency compared to that of the baseline for the SOEC operation, suggesting the changes in the oxygen exchange kinetics within the air electrode for SOEC operations. The processes associated with the characteristic frequencies of 1-150 Hz are commonly attributed to oxygen electrode activation and polarization resistance, particularly during the oxygen evolution reaction.[45]

The shift in P4 frequency after infiltration can be explained by enhanced oxygen surface exchange and oxygen ion transport within the air electrode, which is facilitated by the modified electrode microstructure and chemistry introduced by $SrFe_2O_{4-d}$. The infiltration appears altering the surface activity of the LSM backbone by providing additional active sites for oxygen exchange while reducing the activation energy for oxygen ion migration. Additionally, the structural changes caused by the infiltration reduce the polarization resistance, especially in the 100–200 Hz range, which is associated with oxygen transport processes.

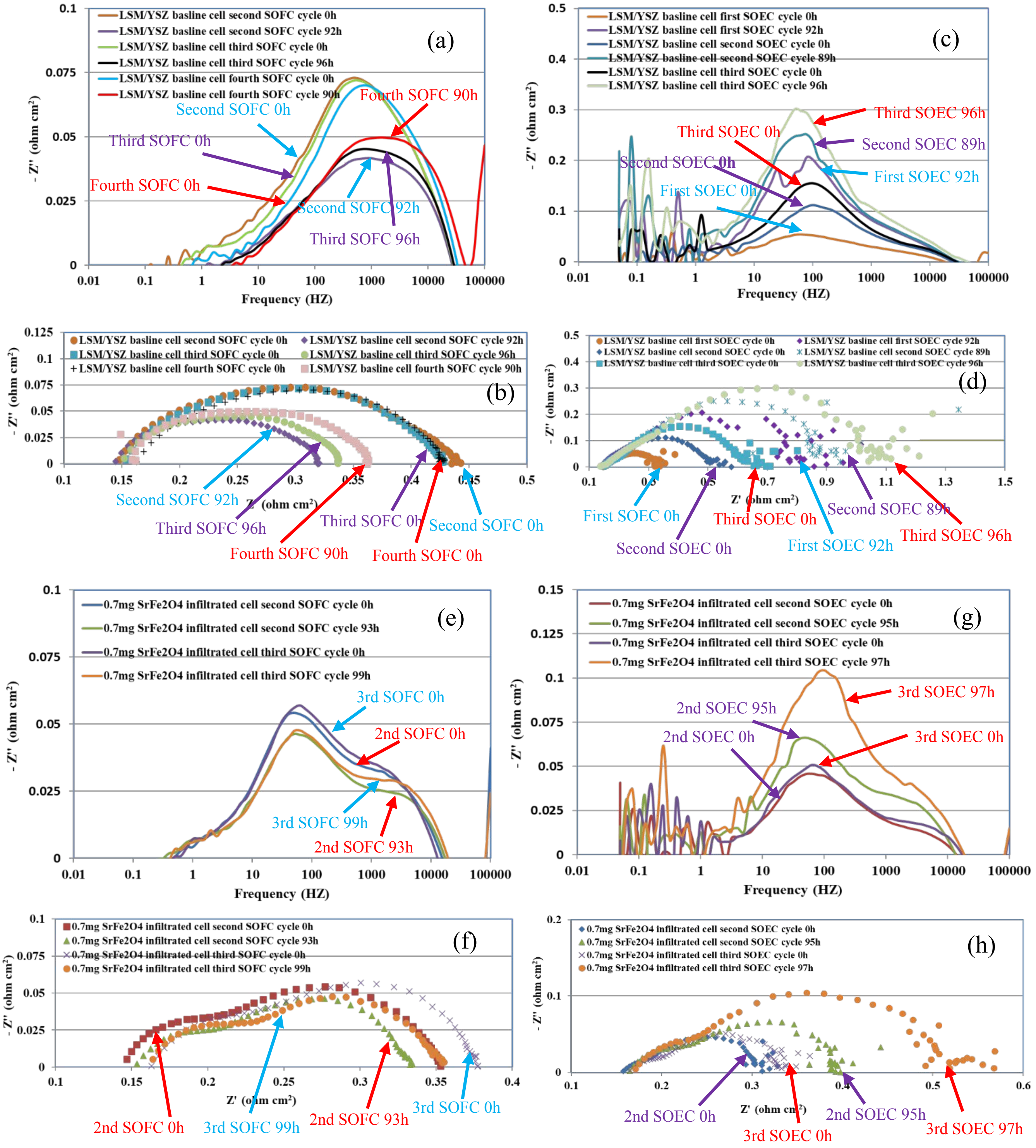

Fig. 8 EIS spectra of the SOFC and SOEC cycles for the LSM/YSZ baseline and infiltrated cells under the R-SOFC/SOEC operation: (a) Bode plot of the SOFC cycles for the LSM/YSZ baseline cell; (b) Nyquist plot of the SOFC cycles for the LSM/YSZ baseline cell; (c) Bode plot of the SOEC cycles for the LSM/YSZ baseline cell; (d) Nyquist plot of the SOEC cycles for the LSM/YSZ baseline cell; (e) Bode plot of the SOFC cycles for the infiltrated cell; (f) Nyquist plot of the SOFC cycles for the infiltrated cell; (g) Bode plot of the SOEC cycles for the infiltrated cell; (h) Nyquist plot of the SOEC cycles for the infiltrated cell.

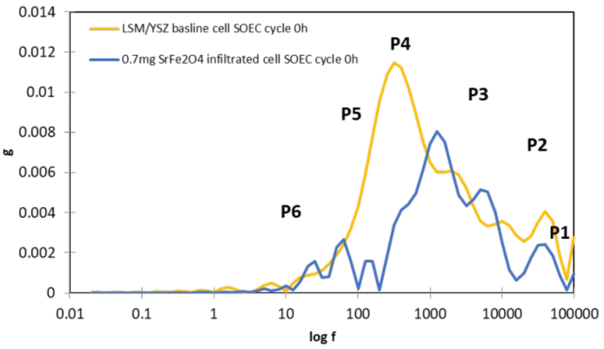

Fig. 9 DRT analysis of LSM/YSZ baseline and $SrFe_2O_{4-d}$ infiltrated cells under SOEC 0h conditions.

Importantly, the consistent operation of the baseline and infiltrated cells under identical conditions highlights the direct influence of $SrFe_2O_{4-d}$ infiltration on electrode performance. While the fuel electrode structures remain unchanged, the observed decrease in the P4 arc for the infiltrated cell further supports the hypothesis of improved ionic and electronic transport. These enhancements likely stem from the infiltration-induced changes in the LSM chemistry, leading to improved oxygen ion conductivity and expanding the catalytic reaction sites to the surface of the LSM grains.

The observed shifts in DRT peaks, particularly the reduction and frequency shift of the P4 arc, provide strong evidence for the beneficial effects of $SrFe_2O_{4-d}$ infiltration. These changes enhance oxygen surface exchange and ion transport, leading to significant reductions in polarization resistance and overall improved electrochemical performance of the LSM/YSZ air electrode.

Beneficial chemistry changes after nanoparticle infiltration in the air electrode

The delamination of the air electrode from the electrolyte has generally been attributed to the low ionic conductivity in LSM and the cracks caused by high oxygen pressure buildup at the electrolyte/air electrode interface, as reported in previous studies.[14-18, 46] This phenomenon was also observed in the current research, as shown in the SEM/TEM images. The formation of microstructural defects, pores, and cracks at the electrode/electrolyte interface further reduced the electrochemically active area. This aligns with the current findings, which show a significant increase in ohmic resistance during the SOEC cycle. Additionally, a notable rise in polarization resistance was observed in the baseline cell after four cycles of R-SOFC/SOEC operation, ultimately leading to complete delamination and catastrophic failure of the LSM/YSZ baseline cell.

For the infiltrated cells, interdiffusion between the infiltrates and the backbone is typically unfavourable in standard solution infiltration processes. However, in this study, the $SrFe_2O_{4-d}$ infiltrates exhibited a beneficially strong interaction with the LSM backbone. Iron from the infiltrates diffused into the LSM backbone, transforming the low oxygen ion-conducting LSM into a Fe-doped LSM mixed conductor, which could help reduce electrode delamination. The interaction between Sr, Fe, and the LSM backbone is primarily driven by high-temperature operations of SOFC and SOEC operations, which facilitates the diffusion of these elements into the perovskite lattice. This process is thermodynamically favourable, as it reduces the system's Gibbs free energy, leading to the formation of Fe-doped LSM. The high-temperature environment allows Sr and Fe to interact with the perovskite lattice, forming La-Sr-Mn-Fe (LSMF) compounds. The diffusion of Sr and Fe into the LSM structure also occurs due to concentration gradients and their high ionic mobility under elevated temperatures. Additionally, the generation of oxygen vacancy during operation enhances ion transport pathways, further facilitating the diffusion process. These factors collectively enable the incorporation of Sr and Fe into the LSM backbone, resulting in a modified microstructure and composition.

The improvement in ionic conductivity of Fe-doped LSM compared to pure LSM is demonstrated by the performance of the $SrFe_2O_{4-d}$ infiltrated LSM/YSZ cell, which exhibited no delamination of air electrode. However, the electronic conductivity of Fe-doped LSM is influenced by both the Fe doping level and operating temperature. While Fe doping typically enhances electronic conductivity by introducing additional charge carriers, it can also affect ionic conductivity by altering the defect chemistry of the material.

Previous studies have shown that Fe doping levels of 20% and 40% in LSM resulted in lower electronic conductivity compared to undoped LSM.[47] However, the lower Fe doping levels employed in this research demonstrated improved electronic conductivity, as evidenced by the reduction in ohmic resistance during the first SOFC cycle. Precise measurements of electronic conductivity depend on the specific doping level and require experimental validation for the individual compositions. It is important to note that this study does not focus on detailed investigations of the electronic and ionic conductivity variations caused by Fe doping. These aspects fall outside the scope of this research and will not be addressed further in this paper.

Simultaneously, La and Mn from the LSM backbone interacted with the $SrFe_2O_{4-d}$ infiltrates, resulting in the formation of Mn-Fe enriched La-Sr-Mn-Fe nanoparticles in the original pores of the air electrode. These nanoparticles not only increased the TPBs but also enhanced the oxygen ionic pathways. The positive interaction between the infiltrates and the LSM backbone significantly reduced pressure buildup at the electrolyte/electrode interface. It mitigated crack formation, improving the reversibility and durability of the infiltrated cells during R-SOFC/SOEC operation. Oxygen exchange occurred at the surface of these materials when Fe and Mn diffusion took place, which would immediately affect oxygen exchange kinetics. This increased ionic conductivity likely extended the reaction sites from the original TPBs to the entire surface of the LSM, contributing to reduced delamination and enhanced durability in the infiltrated cells.

Outlook

LSM and LSCF are commonly used air electrode materials for SOFC operation. LSCF possesses high catalytic activity and good ionic and electronic conductivity. However, the primary concern for the practical application of LSCF cathodes is its long-term performance instability due to Sr segregation under the SOFC operation, LSCF decomposition (formation of Co-Fe) under the SOEC operation, reaction with the YSZ-based electrolytes leading to the application of a barrier layer that caused the complicated and cost ineffective fabrication procedure. The most challenging concern for the SOEC application of the LSM/YSZ-based cell is the electrode's delamination from the electrolyte due to the pressure buildup in the electrode/electrolyte interface induced by the lower oxygen ion conductivity of the LSM backbone. LSM is mainly an electronic conductor with limited ionic conductivity. As a result, oxygen ions produced at the cathode tend to accumulate at the interface, causing a local pressure buildup. Additionally, the OER on the LSM surface is less efficient due to its lower catalytic activity compared to materials with mixed ionic-electronic conductivity. This inefficiency exacerbates the accumulation of oxygen, leading to mechanical stress and possible microstructural damage. These challenges highlight the importance of infiltrating materials like $SrFe_2O_{4-d}$, which can enhance both ionic conductivity and catalytic activity to address these issues.

In these current studies, nanoparticle infiltration in the air electrodes of the LSM/YSZ-based cells has been demonstrated as a simple, promising, and cost-effective way to prevent delamination of the electrode from the electrolyte. The nanoparticle infiltration in the air electrode not only improved the performance and mitigated performance degradation for the LSM/YSZ-based cells, especially for the SOEC cycle, but also extended the durability of the R-SOFC/SOEC. Infiltration permanently improved the backbone structure and possibly induced ionic conductivity in the electrical conductor LSM. Ionic conductivity is needed for LSM. Therefore, the infiltration provides a permanent solution to ultimately solve the problem of delamination, which is very encouraging.

The nanoparticles that formed on the LSM/YSZ backbone were composed of $SrFeO_x$, with La and Mn dopants on the Sr and Fe sites, respectively. Both $SrFeO_x$ and Ti-doped $SrFeO_x$ are known electrocatalysts. The $Sr(Ti_{1-x}Fe_x)O_{3-d}$ electrode exhibits low polarization resistance and excellent stability at 700 °C during both the SOFC and SOEC operations, making it competitive, or even superior to other mixed ionic-electronic conducting (MIEC) electrodes such as LSCF.[48] Although the specific effects of La and Mn doping on the $SrFeO_x$ in this study are not fully understood, it is likely these particles provide additional electrocatalytic activity for OERs during the SOEC operation. Most importantly, the particles serve as a cation reservoir, supplying Fe to the LSM to enhance its ionic conductivity. With continuous operation, the chemical composition of the particles is expected to stabilize, and they may eventually become Mn-enriched rather than Fe-enriched. While there is still some degradation after the infiltration of $SrFe_2O_{4-d}$, optimizing the chemical composition of the solutions, such as adjusting the Sr : Fe ratio or introducing different doping elements, could further improve H_2 production during SOEC cycle operation.

Summary

The $SrFe_2O_{4-d}$ infiltration in the air electrode clearly improved the cell's overall performance, mitigated performance degradation, and extended the cell's operational duration, at increased hydrogen production rate, without delamination of the air electrode for the R-SOFC/SOEC test. The EIS analysis showed that the $SrFe_2O_{4-d}$ solution infiltration in the air electrode decreased both of the initial ohmic/polarization resistance, which resulted in improved initial performance. However, the ohmic/polarization resistance increased with more R-SOFC/SOEC operational cycles, especially for the polarization resistance. This resulted in performance degradation, with the SOEC cycles contributing the most to the performance degradation. The air electrode was totally delaminated in the LSM/YSZ baseline cell. The $SrFe_2O_{4-d}$ nanoparticle infiltration in the air electrode appeared to inhibit delamination. This might be attributed to an increase in TPBs and improved oxygen ion conductivity of the air electrode by the infiltrated $SrFe_2O_{4-d}$ nanoparticles, which may have quelled the oxygen partial pressure in the air electrode. The SEM studies on the $SrFe_2O_{4-d}$ infiltrated cell showed no delamination in the air electrode from the electrolyte. The TEM studies on the H_2 electrode revealed the formation of NiO in both the $SrFe_2O_{4-d}$ infiltrated and LSM/YSZ baseline cells after the R-SOFC/SOEC test. The formation of NiO and Ni migration to the original pore region may have led to performance degradation. However, NiO could be reduced back to Ni during the SOFC cycles, which can explain why the SOFC operation mode reversed some performance loss observed during the SOEC operation in the R-SOFC/SOEC test. Even though a SOFC cycle could reverse some performance loss observed during the SOEC cycles, nonconductive second-phase formation, microstructure change, or even fracture is irreversible, which can contribute to performance degradation of both the baseline and infiltrated cells. The reversibility is attributed to the reduced electrode resistance and enhanced catalytic activity that is simultaneously introduced to the electrode backbone through the strong interaction between the infiltrate and the backbone. The present study opens new research directions of modifying and improving the electrochemical activity of the electrode of inherently functional cells through the infiltration of the solutions with different chemistry.

Data availability

The authors confirm that the data supporting the findings of this study are available within the article and its ESI.

Author contributions

Y. F: performed the experiment and data analysis, wrote/reviewed/edited the manuscript with inputs from all authors. Y. C: SEM/TEM studies. R.P: resources, assisted equipment setup. H. A: project leader, funding acquisition and project administration. X. S: SEM/TEM studies and reviewed/edited the manuscript. T. K: project administration.

Conflicts of interest

There are no conflicts of declare.

Disclaimer

This project was funded by the United States Department of Energy, National Energy Technology Laboratory, in part, through a site support contract. Neither the United States Government nor any agency thereof, nor any of their employees, nor the support contractor, nor any of their employees, makes any warranty, express or implied, or assumes any legal liability or responsibility for the accuracy, completeness, or usefulness of any information, apparatus, product, or process disclosed, or represents that its use would not infringe privately owned rights. Reference herein to any specific commercial product, process, or service by trade name, trademark, manufacturer, or otherwise does not necessarily constitute or imply its endorsement, recommendation, or favoring by the United States Government or any agency thereof. The views and opinions of authors expressed herein do not necessarily state or reflect those of the United States Government or any agency thereof.

References

1 M. B. Mogensen, M. Chen, H. L. Frandsen, C. Graves, J. B. Hansen, K. V. Hansen, A. Haunch, T. Jacobsen, S. H. Jensen and T. L. Skafte, Clean Energy, 2019, **3**, 175-201.

2 Y. Yang, S. Bremner, C. Menictas, M. Kay, Renewable and Sustainable Energy Reviews, 2018, **91**, 109-125.

3 J. Zhou, N. Wang, J. Cui, J. Wang, J. Yang, Z. Zong, Z. Zhang, Q. Chen, X. Zheng, K. Wu, Journal of Alloys and Compounds, 2019, **792**, 1132-1140.

4 M. Mogensen, Current Opinion in Electrochemistry, 2020, **21**, 265-273.

5 M. Khan, X. Xu, R. Knibbe, Z. Zhu, Renewable and Sustainable Energy Reviews, 2021, **143,** 110918.

6 P. D. Giorgio, U. Desideri, Energies, 2016, **9**, 662-676.

7 G. Jung, C. Chang, C. Yeh, X. Nguyen, S. Chan, C. Lin, J. Yu, W. Lee, S. Chang, I. Kao, International Journal of Hydrogen Energy 2016, **41**, 21802-21811.

8 Y. Wang, A. Banerjee, L. Wehrle, Y. Shi, N. Brandon, O. Deutschmann, Energy Conversion and Management 2019, **196**, 484–496.

9 R. Knibbe, M.L. Traulsen, A. Hauch, S.D. Ebbesen, M. Mogensen, Journal of The Electrochemical Society, 2010, **157(8)**, B1209-B1217.

10 T. Cheng, Y. Lei, Y. Chen, Y. Fan, H. Abernathy, X. Song, Y. Wen, Journal of Power Sources, 2023, **569**, 232991.

11 M. P. Hoerlein, M. Riegraf, R. Costa, G. Schiller, K. A. Friedrich, Electrochimica Acta, 2018, **276**, 162-175.

12 M.B. Mogensen, A. Hauch, X. Sun, M. Chen, Y. Tao, S.D. Ebbesen, K. V. Hansen, P. V. Hendriksen, Fuel Cells, 2017, **17**, 434–441.

13 A. Hauch, S.D. Ebbesen, S.H. Jensen, M. Mogensen, Journal of The Electrochemical Society, 2008, **155**, B1184–B1193.

14 J. R. Mawdsley, J. D. Carter, A. J. Kropf, B. Yildiz, V. A. Maroni, International Journal of Hydrogen Energy 2009, **34**, 4198-4207.

15 A. Kaiser, E. Monreal, A. Koch, D. Stolten, Ionics, 1996, **2**, 184-189.

16 K. Chen, S. Jiang, International Journal of Hydrogen Energy, 2011, **36**, 10541-10549.

17 V. Brichzin, J. Fleig, H.U. Habermeier, G. Cristiani, J. Maier, Solid State Ionics, 2002, **152**, 499-507.

18 J. Mizusaki, T. Saito, H. Tagawa, Journal of the Electrochemical Society, 1996, **143**, 3065-3073.

19 A. V. Virkar, International Journal of Hydrogen Energy, 2010, **35**, 9527-9543.

20 M. A. Laguna-Bercero, V. M. Orera, International Journal of Hydrogen Energy, 2011, **36**, 13051-13058.

21 Y. Fan, Y. Chen, H. Abernathy, R. Pineault, R. Addis, X. Song, G. Hackett, T. Kalapos, Journal of Power Sources, 2023, **580**, 233389.

22 J. Malzbender, R. Steinbrech, Journal of Power Sources, 2007, **173**, 60-67.

23 Y. Fan, X. Song, H. Abernathy, Y. Chen, R. Pineault, J. Liu, K. Gerdes, S. Lee, T. Kalapos, G. Hackett, ECS Transactions, 2017, **78**, 1003.

24 Y. Fan, Y. Chen, H. Abernathy, R. Pineault, X. Song, J. Liu, K. Gerdes, S. Lee, T. Yang, T. Kalapos, ECS Transactions, 2018, **85**, 1277.

25 S. Lee, M. Bevilacqua, P. Fornasiero, J. M. Vohs, R. J. Gorte, Journal of Power Sources 2009, **193**, 747-753.

26 P. Wu, Y. Tian, Z. Lü, X. Zhang, L. Ding, International Journal of Hydrogen Energy, 2022, **47**, 747-760.

27 P. Qiu, X. Yang, L. Zou, T. Zhu, Z. Yuan, L. Jia, J. Li, F. Chen, ACS Appl. Mater. Interfaces, 2020, **12**, 29133–29142.

28 M. M. Welander, B. Hu, M. C. Tucker, International Journal of Hydrogen Energy, 2023, **48**, 21578-21585.

29 T. Ishihara, Z. Tan, J. Song, A. Takagaki, Solid State Ionics, 2022, **379**, 115914.

30 C.H. Yang, C. Jin, A. Coffin, F.L. Chen, International Journal of Hydrogen Energy, 2010, **35**, 5187-5193.

31 C.H. Yang, A. Coffin, F.L. Chen, International Journal of Hydrogen Energy, 2010, **35**, 3221-3226.

32 H. Fan, Y. Zhang, M. Han, Journal of Alloys and Compounds, 2017, **723**, 620-626.

33 Y. Tan, S. Gao, C. Xiong, B. Chi, International Journal of Hydrogen Energy, 2020, **14**, 19823-19830.

34 B. Bibi, A. Nazar, B. Zhu, F. Yang, M. Yousaf, R. Raza, M. Shah, J. Kim, M. Afzal, Y. Lei, Y. Jing, P. Lund, S. Yun, Advanced Powder Materials, 2024, **3**, 100231.

35 P. Wu, Y. Tian, Z. Lu, X. Zhang, L. Ding, International Journal of Hydrogen Energy 2022, **47**, 747-760.

36 K. Zhao, J. Lu, L. Le, C. Coyle, O. Marina, K. Huang, Applied Energy 2024, **361**, 122962.

37 H. Shimada, Y. Fujimaki, Y. Fujishiro, Ceramics International, 2020, **46 (11)**, 19617-19623.

38 Y. Chen, H. Abernathy, G. Hackett, Y. Fan, S. Lee, K. Gerdes, X. Song, Acta Materialia, 2022, **237**, 118179.

39 T. Cheng, Y. Lei, Y. Chen, Y. Fan, H. Abernathy, X. Song, Y. Wen, Journal of Power Sources, 2023, **569**, 232991.

40 C. Graves, S. Ebbesen, S. Jensen, S. Simonsen, M. Mogensen, Nature Materials, 2015, **14**, 239–244.

41 V. Sonn, A. Leonide, E. Ivers-Tiffée, Journal of The Electrochemical Society, 2008, **155**, B675-B679.

42 B. Liu, H. Muroyama, T. Matsui, K. Tomida, T. Kabata, K. Eguchi, Journal of The Electrochemical Society, 2010, **157**, B1858-B1864.

43 R. Barfod, M. Mogensen, T. Klemenso, A. Hagen, Y. Liu, P. Vang Hendriksen, Journal of the Electrochemical Society, 2007, **154**, 371-378.

44 A. Leonide, B. Ruger, A. Weber, W.A. Meulenberg, E. Ivers-Tiffee, Journal of the Electrochemical Society, 2010, **157**, B234-B239.

45 M. Kornely, A. Neumann, N.H. Menzler, A. Leonide, A. Weber, E. Ivers-Tiffee, Journal of Power Sources, 2011, **196**, 7203-7208.

46 A. Momma, T. Kato, Y. Kaga, S. Nagata, J. Ceram. Soc. Jpn., 1997, **105 (5)**, 369–373.

47 S. Kuharuangrong, T. Dechakupt, P. Aungkavattana, Materials Letters, 2004, **58**, 1964-1970.

48 L. dos Santos-Gómez, J. M. Porras-Vázquez, E. R. Losilla, D. Marrero-López, RSC Adv., 2015, **5**, 107889–107895.

Data availability

The authors confirm that the data supporting the findings of this study are available within the article and its ESI.